

www.acsaem.org Article

Direct Laser Writing of Multimetal Bifunctional Catalysts for Overall **Water Splitting**

Shannon McGee, Andres Fest, Cierra Chandler, Nabila N. Nova, Yu Lei, James Goff, Susan B. Sinnott, Ismaila Dabo, Mauricio Terrones,* and Lauren D. Zarzar*

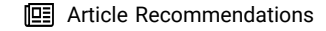


Cite This: ACS Appl. Energy Mater. 2023, 6, 3756-3768



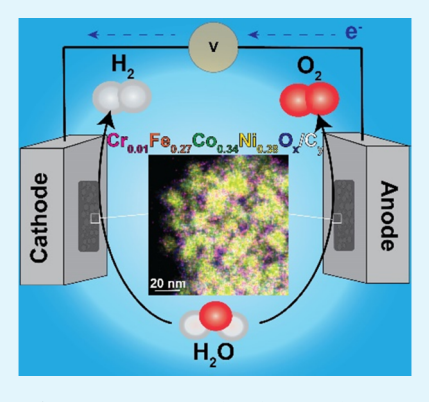
ACCESS I

Metrics & More



Supporting Information

ABSTRACT: Water electrolysis is of interest as a sustainable way to produce clean hydrogen and oxygen fuel and help mitigate the rising problems of climate change while meeting global energy demands. High-efficiency, stable, and earth-abundant bifunctional catalysts are needed to enable more effective electrochemical cells for the hydrogen evolution reaction (HER) and oxygen evolution reaction (OER). Here, we investigate the synthesis, composition, performance, and mechanism of multimetal catalysts serving dual functionality in both OER and HER of water electrolysis. Through a laser synthesis method, we synthesized heterogeneous catalysts of nanocrystalline multimetallic alloy pockets embedded within an amorphous oxide matrix. We evaluated the performance and composition of a range of mixed transition-metal oxide materials for both OER and HER, ultimately synthesizing a $Cr_{0.01}Fe_{0.27}Co_{0.34}Ni_{0.38}O_x/C_v$ catalyst that has a stable, high-rate, and competitive overall water splitting performance of 1.76 V at 100 mA cm⁻² in an alkaline medium. Using density functional theory to gain insight as the active site and



mechanism, we propose that the inclusion of a minor amount of Cr increases the degeneracy of energetic states that lowers the cost of forming the O 2 p-d bond and H 1 s-d bond due to the hybridization of s, p, and d orbitals from Cr. Using a two-electrode water electrolysis cell with a constant potential of 1.636 V to mimic the setup for fuel production, we found the catalyst to be stable at 14-15 mA cm⁻² for 40 h. This laser synthesis method allowing for facile and rapid synthesis of complex multimetal systems demonstrates how doping a Fe, Co, and Ni heterogeneous amorphous/nanocrystalline structure with small amounts of Cr is important for bifunctional catalytic behavior, particularly for increasing HER functionality in advancing our understanding for future electrocatalytic design.

KEYWORDS: laser writing, multimetal catalysis, oxygen evolution reaction, hydrogen evolution reaction, water splitting, transition-metal oxides, nanostructured materials

INTRODUCTION

Due to increasing global energy demands, the depletion of nonrenewable fossil fuels, and the negative impacts of climate change, it is imperative to quickly find clean and renewable energy sources for the future. The electrolytic splitting of water to produce hydrogen and oxygen fuel provides a clean and renewable energy resource and has drawn significant attention for research and application interest.^{2,3} Common examples of monofunctional hydrogen evolution reaction (HER) and oxygen evolution reaction (OER) catalysts are Pt- and Ru/Ir-based catalysts that have, respectively, overpotentials of \sim 30 to 50 and 250 mV at 10 mA cm⁻² in alkaline media.^{4,5} As the theoretical minimum voltage difference to drive the overall electrolysis of water is 1.23 V,6 the practical cell voltage using the aforementioned monofunctional catalysts would be $\sim 1.53 \text{ V}$ at 10 mA cm⁻² in the absence of any loss of efficiency. Improvements in catalyst stability, reaction rates, efficiency of cell designs, and reduction in cost (e.g., replacement of precious metals) are urgently needed.^{7,8} If a single, nonprecious, bifunctional catalyst could be used for

both HER and OER in alkaline electrolyte without poisoning each other due to ion dissolution, then a more cost-effective, efficient single-chamber, two electrode electrolytic cell could be used instead. 9-11

Recently, research efforts have focused on developing earthabundant mixed transition-metal catalysts for water splitting, both because such metals are more sustainable but also because they have modulated d-orbitals resultant from the multimetal catalyst structure $^{12-16}$ that leads to better HER and OER catalytic performance. Density functional theory (DFT) investigations of the performance of multimetal catalysts for water splitting have also shown, for example, that NiOOH materials doped with Cr, Mn, Fe, Co, Cu, or Zn can influence

Received: December 9, 2022 Accepted: March 13, 2023 Published: March 24, 2023





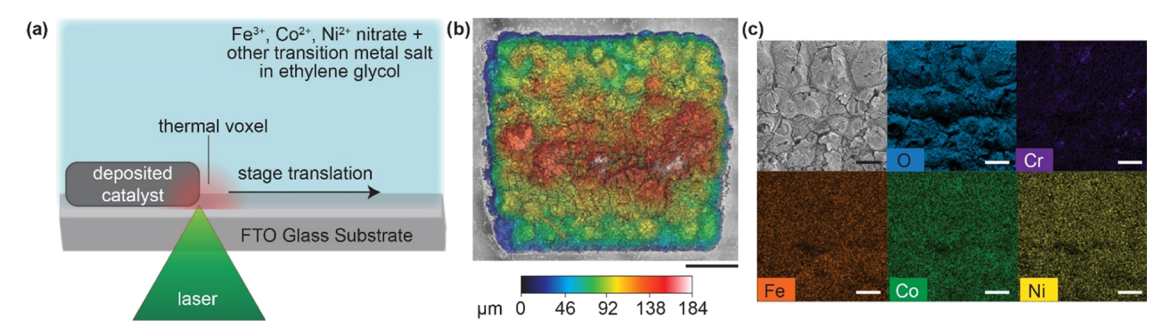


Figure 1. Laser-induced thermal voxel (LITV) synthesis of overall water splitting catalysts. (a) Schematic of the LITV synthesis method; a continuous wave laser (532 nm) is focused through an objective lens onto the surface of a fluorine-doped tin oxide (FTO) glass substrate covered with a $60-80~\mu$ L droplet of fluid precursor of transition-metal salts dissolved in ethylene glycol. Absorption of the laser produces a steep, localized thermal gradient, i.e., "thermal voxel" to thermally decompose precursors and pattern a solid material for catalysis. Precursors used were 1 M transition-metal hydrate salts in ethylene glycol solvent. All transition-metal salts utilized are described in the Methods section. (b) Profilometry image of an exemplary multimetal catalyst, patterned in a 1×1 mm square, with thickness according to the color scale. Scale bar is $250~\mu$ m. (c) Top left: scanning electron micrograph (SEM) of a selected area of the catalyst in (b). All others: energy-dispersive X-ray spectroscopy (EDS) maps show a mixed material containing O, Cr, Fe, Co, and Ni. Scale bar is $100~\mu$ m.

the binding energies of hydrogen and oxygen adsorption due to orbital hybridization. 17,18 Experimentally, multimetal catalysts with transition-metal combinations including Co, Ni, or Fe have been found to have application for overall water splitting with improved stability in HER and OER; however, many of these catalysts are still not competitive for overall water splitting at higher current densities, with most only studies reporting values at 10 mA cm⁻² with practical cell voltages of falling in the range of 1.42-2.1 V (Table S1). 14,15,19-24 To advance our understanding of how these synergistic properties in multimetal materials affect water splitting catalytic behavior, we utilize a laser-induced thermal voxel (LITV) method for synthesizing and patterning a wide range of nanocrystalline transition multimetal catalysts from fluid precursors. 25-30 In this method, a laser is focused onto the interface between a substrate and precursor solution containing an optical absorber; the photothermal response at the focus heats a microscale volume of solution to temperatures reaching over 1000 °C, which induces solvothermal reactions and decomposition to yield nanomaterial composites. This LITV method offers the advantage of being able to easily vary the synthesis parameters such as precursor chemicals and composition, solvent, and laser power to affect the chemical and structural properties in the resulting mixed-metal catalyst. 25-27,30 Recently, we demonstrated the utility of this method for facile one-step synthesis and patterning of OER catalysts composed of Fe, Co, and Ni oxides.^{25,27}

Here, we demonstrate the LITV synthesis of multimetal catalysts with varying compositions of Fe, Co, Ni, and a fourth transition-metal dopant (Ti, V, Cr, Mn, Co, Zn, Mo, or W) for overall water splitting applications. Cr doping led to the best stable, bifunctional catalyst, with the composition $Cr_{0.01}Fe_{0.27}Co_{0.34}Ni_{0.38}O_x/C_y$ having HER and OER overpotentials at 100 mA cm⁻² of 214 \pm 11 and 318 \pm 4 mV, respectively, bringing the practical cell voltage of the theoretical electrolytic cell to 1.76 \pm 0.01 V. We used Kohn—Sham DFT to demonstrate how in Cr-doped Fe, Co, and Ni multimetal oxide systems, adding a minor amount of Cr can increase the H binding affinity of the catalyst, effectively functionalizing the material for HER. Structural characterization of the $Cr_{0.01}Fe_{0.27}Co_{0.34}Ni_{0.38}O_x/C_y$ catalyst shows a complex heterogeneous nanoscale structure composed of metallic nanoparticles within an amorphous oxide matrix.

Annealing reduced catalytic performance, suggesting that the structural interface between the amorphous oxide and metallic crystalline nanostructures is critical to lowering HER overpotentials. Using a two-electrode, single-chamber water electrolysis cell with a constant potential of 1.636 V to mimic the setup for fuel production, the dual catalyst system for overall water splitting exhibited stability at 14-15 mA cm⁻² for 40 h. This work demonstrates that LITV is a powerful method for screening and studying bifunctional catalytic material with complex structures for overall water electrolysis and provides insight into the mechanistic principles governing multimetal catalysis design and structure-activity relationships. Through this study, we advance our understanding for future design of cost-effective, high-rate, stable, water electrolysis multimetal catalysts for renewable energy applications.

■ RESULTS AND DISCUSSION

To utilize the LITV synthesis method for catalyst production, we focused a 532 nm continuous wave laser through an objective lens into a precursor salt solution to create a hightemperature (>1000 °C) solvothermal micro-reactor, dubbed a thermal voxel (Figures 1a and S1).²⁵⁻³⁰ Thermal decomposition of the precursor solution within the thermal voxel generated nanoparticles in situ, which were sintered to the substrate in a film as the laser was scanned. 25,26,29 Generally, our precursors used in this work were 1 M solutions of mixed metal salt precursors dissolved in ethylene glycol, wherein the ratio of the specific salts was tuned to create different multimetal catalyst compositions. For example, an equimolar precursor solution of Fe, Ni, Co, and Cr precursor would be $0.25 \text{ M Fe}(NO_3)_3$, $0.25 \text{ M Ni}(NO_3)_2$, $0.25 \text{ M Co}(NO_3)_2$, and 0.25 M Cr(NO₃)₃ in ethylene glycol. Ethylene glycol was used as the solvent to enhance the porosity of the material and increase surface area as seen by scanning electron microscopy (SEM) (Figure S2). 25,26 For any given precursor, we used the LITV method to synthesize a $1 \times 1 \text{ mm}^2$ catalyst square on a fluorine-doped tin oxide (FTO) glass substrate for catalytic testing. The surface area of the catalyst square was estimated using optical profilometry (Figure 1b). Since there is often not a one-to-one correlation between the input molar ratio of the metal ions in the precursor solution to the output ratio of elements in the catalyst, 27 energy-dispersive X-ray spectrosco-

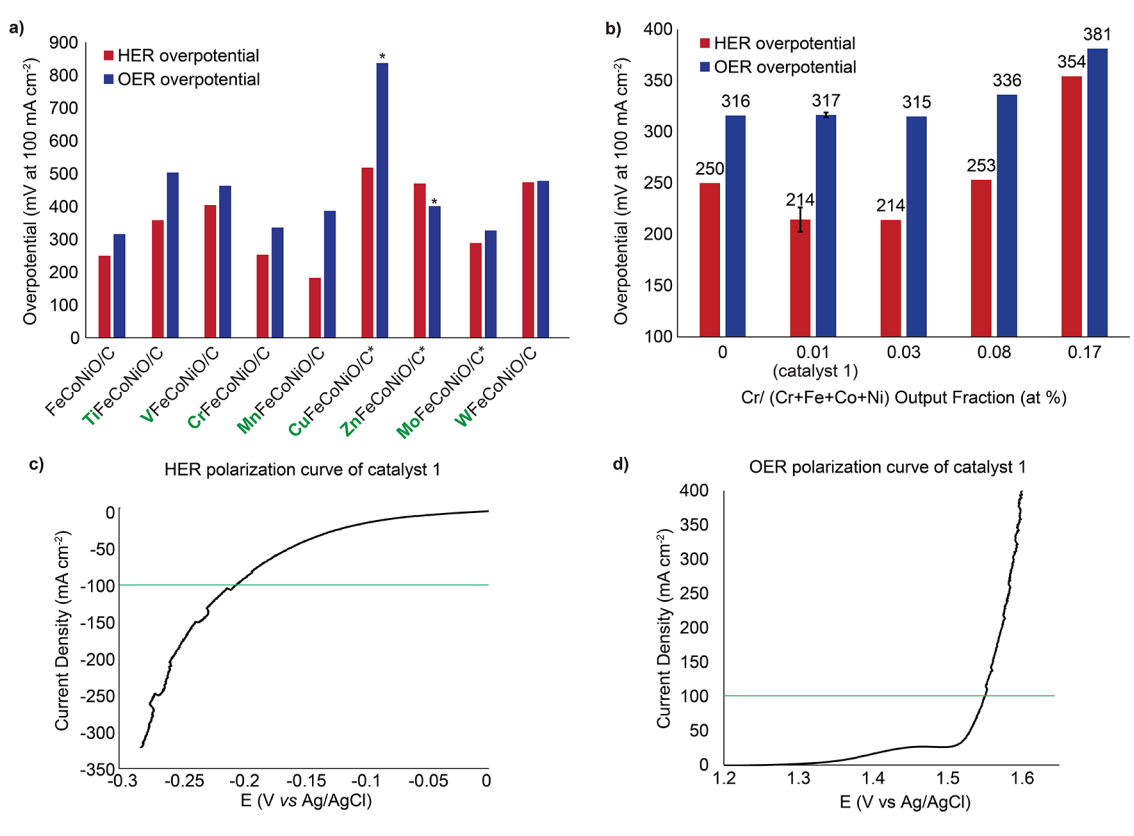


Figure 2. HER and OER performance of LITV synthesized catalysts for overall water splitting. (a) HER and OER overpotentials of catalysts containing a range of transition-metal compositions, prepared using precursor solutions containing an equimolar ratio of each element. Current density was 100 mA cm⁻². FeCoNiO_x/C_y was used as the "base" to which a fourth transition metal was added. An asterisk (*) marks an unstable catalyst. Each catalyst's performance and elemental output composition are described in more detail in Table S2. (b) HER and OER overpotential of catalysts with increasing Cr content measured at a current density of 100 mA cm⁻². The best bifunctional catalyst had overpotentials of 214 \pm 11 and 318 \pm 4 mV for HER and OER, respectively (catalyst 1). Catalyst 1's output composition was Cr_{0.01}Fe_{0.27}Co_{0.34}Ni_{0.38}O_x/C_y as determined by EDS (Table S5); the input elemental ratio was Cr_{0.1}Fe₁Co₁Ni₁. Each catalysts' elemental input ratios, output fractions (atom %), and electrochemical performance are described in detail in Tables S2–S5. (c) HER polarization curve of catalyst 1. The overpotential is 210 mV at -100 mA cm⁻². (d) OER polarization curve of catalyst 1. The overpotential is 322 mV at 100 mA cm⁻². All overpotential measurements and potential curves are taken from the fourth cycle of LSV after 60× cycles of ECSA and 3 cycles of LSV to ensure activation of the catalyst.

py (EDS) was used to determine the approximate elemental composition of the catalysts (Figure 1c and eq 1). More details about the optical setup, laser scanning parameters, and solution compositions are described in the Methods section and Figure S1.

To test a prepared catalyst, we used a 3-probe testing setup with 1 M KOH electrolyte solution, an Ag/AgCl reference electrode, a graphite or Pt counter electrode, and our synthesized catalyst as the working electrode. For each catalyst, we measured electrochemical active surface area (ECSA) with cyclic voltammetry (CV) at a minimum of 60 cycles, then conducted electric impedance spectroscopy (EIS), followed by 4 cycles of linear sweep voltammetry (LSV) for HER and OER to confirm the activation of the catalyst for overpotential and Tafel slope measurements. Catalysts' overpotentials were compared at current densities of 100 mA cm⁻² both to demonstrate the high-rate water electrolysis performance and also because there was interference of Ni oxidation in the polarization curve at 10 mA cm⁻² (Figure S3). We compared the performance of our catalysts to common monofunctional hydrogen evolution reaction (HER) and oxygen evolution reaction (OER) catalysts that are Pt- and Ru/Ir-based, respectively, that have overpotentials of ~300 and >275 mV at 100 mA cm⁻² in alkaline medium for a ΔV to \sim 1.81 V provided no loss of efficiency.^{4,5} A summary of the precursor

compositions, corresponding elemental output fractions in the catalyst in atom % (eq 1), and electrocatalytic performances are detailed in Tables S2–S5 for all catalysts.

We first analyzed the catalytic performance of our "base" composition, $Fe_{0.53}Co_{0.26}Ni_{0.20}O_x/C_y$, which was synthesized from a precursor solution containing 0.33 M Fe(NO₃)₃, 0.33 M Co(NO₃)₂, and 0.33 M Ni(NO₃)₂ in ethylene glycol; this composition was used because our previous LITV work optimized this composition for OER.²⁷ This catalyst exhibited overpotential performances measured at 100 mA cm⁻² for HER and OER of 250 and 316 mV, respectively, yielding ΔV of 1.80 V, similar to precious metal standards at high current density.^{4,5} As the Fe, Co, and Ni "base" catalyst had already been optimized for OER through previously published work,² we wondered whether adding a fourth transition metal we could improve the catalyst for HER while maintaining OER performance to create an effective catalyst for overall water splitting. 12,14,15 We hypothesized that the addition of the fourth transition metal may alter the amorphous/nanocrystalline structure and d-orbital configurations so as to affect binding affinity and the orbital overlap of the intermediates leading to better overall water splitting potential and stability, particularly to help target better HER overpotentials. 19,2

To study the synergistic effect of adding a fourth transition metal, we synthesized catalysts containing the FeCoNiO_x/C_y

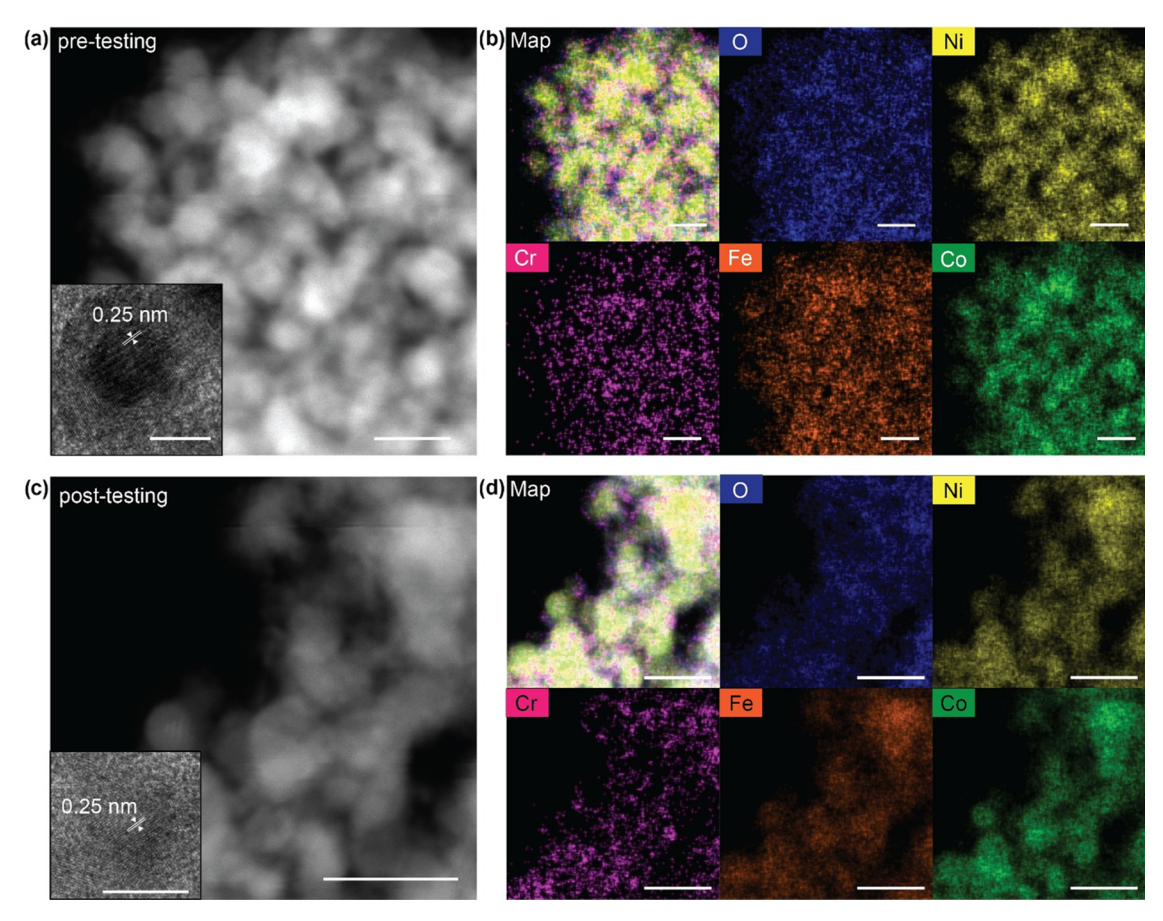


Figure 3. Structural characterization of catalyst 1 before and after HER-OER catalytic testing. (a) STEM with HRTEM inset before HER-OER catalytic testing. HRTEM shows an average lattice spacing of 0.25 nm within the nanoparticle, which is encased in an amorphous matrix. Nanoparticle diameters range from ~5 to 21 nm with most nanoparticles falling in the range of 8–11 nm. Scale bar for STEM is 20 nm. HRTEM inset scale bar is 5 nm. (b) EDS maps showing the distribution of elements in catalyst 1 before testing, O (blue), Ni (yellow), Cr (pink), Fe (orange), and Co (green). Nanoparticle diameter distribution and element distribution analysis shown in Figure S8a,b, respectively. Scale bars in STEM-EDS images are 20 nm. (c) STEM with HRTEM inset after HER-OER catalytic testing. HRTEM shows an average lattice spacing of 0.25 nm within the nanoparticle, which is encased in an amorphous matrix. Nanoparticle diameters range from ~5 to 21 nm with most nanoparticles falling in the range of 9–11 nm (Figure S8a). Scale bar for STEM is 20 nm. HRTEM inset scale bar is 5 nm. (d) EDS maps showing the distribution of elements in catalyst 1 after catalytic testing, O (blue), Ni (yellow), Cr (pink), Fe (orange), and Co (green). Both before and after catalytic testing, the STEM-EDS shows nanoparticles that are enriched in Co and Ni. The amorphous matrix is enriched in Cr and O. Fe is distributed both inside and outside the nanoparticles. Scale bars in STEM-EDS images are 20 nm.

"base combination" with the addition of one other transition metal (e.g., Ti, V, Mn, Cr, Cu, Zn, Mo, or W) wherein equimolar elemental input ratios were used (Figure 2a).²⁷ In Table S2, a summary of the results shows that the addition of the elements Ti, V, Cu, Zn, or W to the "base combination" yield $\Delta V > 2.0 \text{ V}$ at 100 mA cm⁻², which is outside the realm of competitive efficiency for overall water splitting catalysts.^{4,5} Adding Cr, Mn, or Mo led to lower HER overpotentials with overall water splitting $\Delta V < 2.0 \text{ V}$ at 100 mA cm⁻². The ΔV values for CrFeCoNiO_x/C_v, MnFeCoNiO_x/C_v, and MoFeCo-NiO_x/C_y samples were 1.82, 1.80, and 1.85 V, respectively. The HER and OER performances for these combinations were notable to us, as previously studied crystalline binary and ternary multimetal catalyst materials with Cr were only found to be functional for OER while Mo and W containing catalysts had more functionality for HER. 31-34 Using EIS to measure the charge transfer resistance, we observed that the $FeCoNiO_x/C_y$, $CrFeCoNiO_x/C_y$, and $MnFeCoNiO_x/C_y$ had the smallest resistances and TiFeCoNiO_x/C_v and WFeCo- NiO_x/C_y had the largest resistances (Figure S4).

From the data in Figure 2a and Table S2, we identified the catalysts with the most promising performance (CrFeCoNiO_x/ C_y , MnFeCoNiO_x/ C_y , and MoFeCoNiO_x/ C_y). To explore how the synergy of the elements in these three compositions affect overall water splitting, we studied how varying the input precursor ratios (and thus output elemental ratios) in these catalysts affect the catalytic performance (Tables S3-S5). In Table S3, we observed that while some catalysts with Mn, Fe, Co, and Ni variations were able to lower HER overpotential, most of the OER overpotentials increased and became comparatively worse to the ternary FeCoNiO_x/C_v control catalyst. No catalysts incorporating Mn, Fe, Co, and Ni were able to have a competitive ΔV below 1.80 V at 100 mA cm⁻². In Table S4, we found that catalysts with Mo, Fe, Co, and Ni in varying ratios we were able to lower the HER overpotential while keeping the OER overpotential similar to the FeCoNiO_x/C_y control catalyst to have an overall water splitting performance of ΔV 1.77 V. However, during cycling stability tests (Figure S5), it was observed that the best Mocontaining multimetal catalyst, Mo_{0.03}Fe_{0.37}Co_{0.33}Ni_{0.27}O_x/C_y was not stable during OER (Figure S5a-d). XRD spectra

revealed the appearance of MoO_2 after catalyst testing, suggesting that the Mo sites become permanently oxidized (Figure S5e). $^{35-37}$

The catalysts with Cr, Fe, Co, and Ni input variations were able to yield both competitive HER and OER overpotentials while remaining stable during both sides of the water splitting reaction. In Figure 2b and Table S5, we observed that in catalysts with Cr, Fe, Co, and Ni, having very small amounts of Cr in relation to Fe, Co, and Ni (1-3 atom % Cr) led to the best catalytic performances due to the lowering of HER overpotential compared to the FeCoNiO_x/C_y control. EIS and ECSA measurements were analyzed to better understand the electrochemical properties of these catalysts (Figure S6 and Table S5). The best Cr-containing bifunctional catalysts, and the best of all those tested in this work, was made with an input precursor composition of Cr_{0.01}FeCoNi (catalyst 1, Figure S6a, output composition was $Cr_{0.01}Fe_{0.27}Co_{0.34}Ni_{0.38}O_x/C_y$ as determined by EDS). Catalyst 1 had overpotentials measured at 100 mA cm⁻² for HER and OER of 214 \pm 11 and 318 \pm 4 mV, respectively, ΔV of 1.76 V at 100 mA cm⁻², a high ECSA value of 39 \pm 3 mF cm⁻², and a small EIS charge transfer resistance (Figures 2c and S6b and Table S5). The turnover frequency (TOF) of catalyst 1 is estimated at 0.0216 s⁻¹ for OER and 0.0206 s^{-1} for HER (eqs 2-4). Electrochemical analysis showed that with small amounts of Cr, the overpotentials and Tafel slope became lower compared to the FeCoNiO_x/C_v control and thus, more efficient (Figure S6b). ECSA shows a corresponding trend in that the catalysts with minor amounts of Cr compared to the Fe, Co, and Ni elements had higher ECSA values compared to those without Cr or those with a higher amount of Cr (Table S5 and Figure S6c).

Catalyst 1 has a composition of $Cr_{0.01}Fe_{0.27}Co_{0.34}Ni_{0.38}O_x/C_y$ as determined by EDS (Table S5). For comparison, a compositional depth profile was conducted with X-ray photoelectron spectroscopy (XPS) (Figure S7). The catalyst 1 composition determined by the XPS depth profile is $Cr_{0.02}Fe_{0.34}Co_{0.42}Ni_{0.22}O_x/C_y$ on the surface and $Cr_{0.03}Fe_{0.45}Co_{0.35}Ni_{0.17}O_x/C_y$ in the bulk. When comparing the compositions determined by XPS to EDS, we observe some differences in the elemental measurement, although for both analyses Cr is the minority metal constituent while Fe, Co, and Ni are in more comparable amounts. Both EDS and XPS have significant associated error in the measurement (\sim ±5 and ±10%, respectively), along with different focal spot sizes and depth penetrations. ^{38,39} In addition, as to be shown below, the samples themselves also have a heterogeneous structure, which are all factors that contribute to the differences in elemental analysis results.

To better characterize catalyst 1's structure and crystalline properties, we conducted analyses with high-resolution transmission electron microscopy (HRTEM), scanning transmission electron microscopy—energy-dispersive X-ray spectroscopy (STEM-EDS), and X-ray diffraction (XRD) techniques. In Figure 3, STEM and HRTEM show that catalyst 1's heterogeneous structure consists of crystalline nanoparticles in the range of 5–21 nm diameter before and after HER–OER testing (Figure S8a) surrounded by an amorphous matrix. A STEM-EDS line scan before catalyst testing shows localization of the Co and Ni within the nanoparticles and a localization of O and Cr outside the nanoparticles (Figure S8b). We have learned in our previous published analysis of Fe, Co, and Nicontaining catalysts that this type of heterogeneous structure is

important for targeting lower OER overpotentials, and increasing crystallinity of the amorphous matrix or increasing the amount of metallic Fe can negatively affect OER. Thus to the heterogeneous nature, a range of lattice spacing measurements were recorded mostly falling within the 0.20–0.25 nm range. The 0.25 nm lattice measurement shown within the HRTEM inset in Figure 3 falls within normal lattice spacing range for FCC FeCoNi alloys and FCC CrFeCoNi alloys for the (111) plane both before and after HER–OER catalytic testing. As observed in the XRD pattern, the 2θ shifts resemble the FCC CrFeCoNi alloy more closely (Figure S8c). The XRD pattern does not change significantly after catalytic testing of HER and OER (Figure S8c).

To better understand the role of the amorphous matrix and crystalline nanoparticles in catalyst 1, we annealed catalyst 1 samples for 24 h at various temperatures in atmospheric conditions with the hypothesis that annealing would lead to crystallization of the amorphous oxides and potentially increase nanoparticle size. XRD of the annealed 400 °C sample compared to the nonannealed sample (Figure S9a) showed the appearance of crystalline metal oxide signatures (both spinel Fe⁴² and Co oxides, ⁴³ and SnO₂ ⁴⁴ from the FTO glass substrate) along with the FCC metal. 40,41 We used whole pattern fitting with third polynomial background modeling to try to determine the composition of the spinel oxide peaks; however, due to the significant overlap of these signals as they are in the same phase as well as the strain caused by multiple species existing in the structure, the model was not able to make an accurate prediction as shown by the high R/E value of 1.79 of the pattern fitting (Figure S9b). We found that annealing catalyst 1 has minor impact on OER overpotential, but a significant impact on increasing HER overpotential (Figure S9c). With the exception of the sample annealed at 100 °C, the other annealed samples have averages and standard deviations that fall within the ECSA values of the nonannealed samples (Figure S9d), so we believe that the surface morphology and oxidation states of the sites themselves are not changing drastically for these samples. However, the Tafel slopes for both HER and OER of all of the annealed samples are comparatively higher (Figure S9e), and thus show worse performance, than their nonannealed counterparts. This suggests an intrinsic catalytic activity change. In our previous published OER work, we found that annealing a Fe, Co, and Ni-containing catalyst yielded segregated phases of metallic iron, crystalline iron oxide, and FeCoNi FCC alloy nanoparticles, as well as increased OER overpotential;²⁷ in contrast, here, addition of Cr appears to prevent segregation of metallic iron in catalyst 1 which could be the cause for the stable OER overpotential upon thermal annealing. Overall, we draw the conclusion that increasing the crystallinity of the oxide structure and interfering with the amorphous and crystalline nanoparticle interface in the heterogeneous catalysts between the annealed samples worsens the HER catalytic performance compared to the nonannealed samples.^{4,2}

To study the chemical properties such as chemical bonds and oxidation states present in catalyst 1, we conducted Fourier transform infrared spectroscopy (FTIR) and XPS analyses. In catalyst 1's FTIR spectrum (Figure S10), we observe C–O stretching, M–OH stretching, NO₃⁻ stretching, and O–H stretching at 1078, 1344, 1566, and 3249 cm⁻¹, respectively. Some metal oxide stretching might be occurring; however, the poor signal-to-noise ratio of the spectrum leads to a lack of definition in the wavenumber range

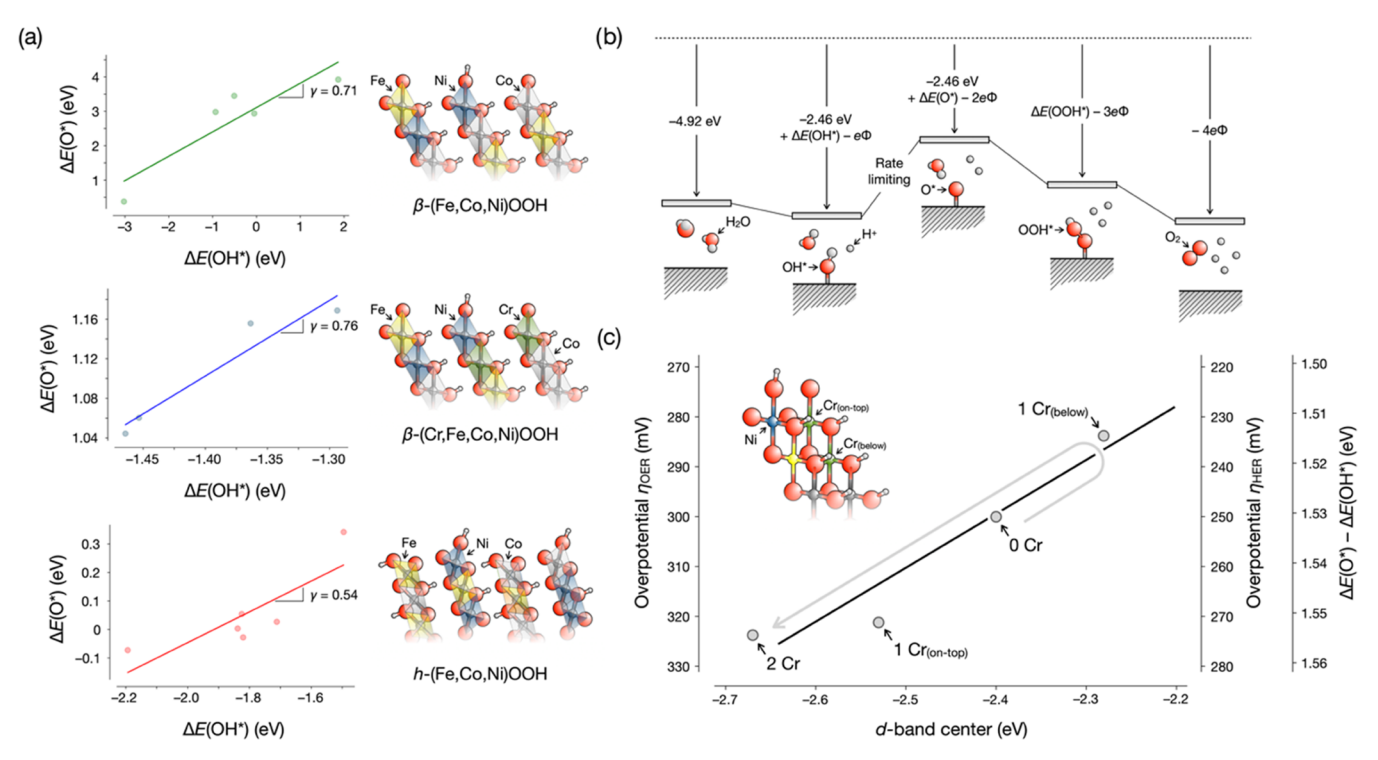


Figure 4. Trends in binding energies and overpotentials for (Cr,Fe,Co,Ni)OOH catalysts. (a) Scaling relationships between $\Delta E(O^*)$ and $\Delta E(OH^*)$ for β -(Fe,Co,Ni)OOH, β -(Cr,Fe,Co,Ni)OOH, and h-(Fe,Co,Ni)OOH, illustrating the moderate influence of local composition and the dominant contribution from crystal structure to the slope γ of the scaling relationship. (b) Surface reaction intermediates as a function of the applied electrode potential Φ. The rate-limiting step is computationally predicted to be the desorption of H* from OH* to form O*. (c) Dependence of the energy difference $\Delta E(O^*) - \Delta E(OH^*)$ and of the overpotentials $\eta_{\rm HER}$ and $\eta_{\rm OER}$ on the (majority-spin) d-band center, showing that placing one Cr below an active Ni site improves electrocatalytic performance while substituting Cr at other neighboring sites decreases HER and OER activities.

of 500-1000 cm⁻¹. XPS analysis was used to supplement these observations and probe the chemical states of the elements on the surface of the catalyst before (Figure S11) and after (Figure S12) HER-OER catalytic testing of catalyst 1. Overall, the analysis shows evidence of metal oxide, metal hydroxide, and metal alloy species before catalyst testing. High-resolution oxygen peaks before and after catalytic testing can be fitted with surface hydroxyl/nonstoichiometric oxygen and lattice oxygen at 530 and 528 eV, respectively. This is due to the mixing of metal oxide and hydroxides creating a nonstoichiometric structure and potential intermediates formed during OER. 27,54-56 XPS shows surface carbon signatures likely originating from the ethylene glycol solvent used in the precursor solution similar to our previous depth profile study (Figure S7) and previous OER work.²⁷ For both catalysts before and after catalytic testing, the Cr 2p, Fe 2p, Co 2p, and Ni 2p core spectra are split into $2p_{1/2}$ and $2p_{3/2}$ orbital peaks due to spin-orbital coupling. S4-56 Similar to our previous work with ternary OER catalysts, Fe and Co 2p core spectra showed evidence for 3+, 2+, and 0 oxidation states suggesting the presence of spinel oxides of Co_3O_4 and Fe_3O_4 along with metallic alloy species on the surface. The Co $2\text{p}_{1/2}$ signal before testing has a dominant species of 2+ and then shifts to a dominant species of 3+ after catalytic testing indicating the oxidation of a Co2+ active site. XPS spectra from both before and after catalytic testing showed a Ni 2p core spectra with 2+ and 0 oxidation states. S4-60 Even though the Ni²⁺ oxidation state is dominant before and after catalytic testing, the metallic alloy species significantly diminishes post-testing suggesting the oxidation of Ni⁰ to Ni²⁺ during catalytic testing. Due to the small amount of Cr in catalyst 1, the signal-to-noise ratio in the core spectra is low; however, there is some evidence suggesting Cr is in the 3+ and 6+ oxidation states before testing and predominantly the 3+ oxidation state after testing. S5,56 There has been literature evidence that Fe³+/2+, Cr⁵+/3+, Co²+, and Ni²+ can be catalytic sites or help facilitate OER and HER intermediate absorption. 9,12,31,54

To elucidate the influence of local structure on the catalytic activity of multimetal oxyhydroxides, we carried out firstprinciples calculations based on the structural models described in Figure S13. Adsorption energies of the reaction intermediates were determined based on previous experimental work demonstrating the formation of oxyhydroxide intermediates during OER for LITV catalysts.²⁷ We predicted the dependence of the overpotential on the filling of the surface d states, taking into account the combinatorial complexity of the atomistic configurations of the most active sites. To address this complexity, we critically examined the scaling relationships that connect the binding energies of the O intermediates $[\Delta E(O^*)]$ to the binding energies of the OH adsorbates $[\Delta E(OH^*)]^{.61}$ This analysis indicated that the scaling relationships $\Delta E(O^*) = \gamma \Delta E(OH^*) + \delta$, which were previously obtained for Fe-, Co-, and Ni-based catalysts, 27 were still applicable to Cr-doped surfaces, albeit with a composition-dependent energy offset δ and a narrower distribution of binding energies. Multiple multimetal combination models were tested for the scaling relationships and detailed in Table S6. Notably, the slope γ of the scaling relationships was found to be moderately affected by Cr doping with a slight increase from 0.71 to 0.76 (Figure 4a).

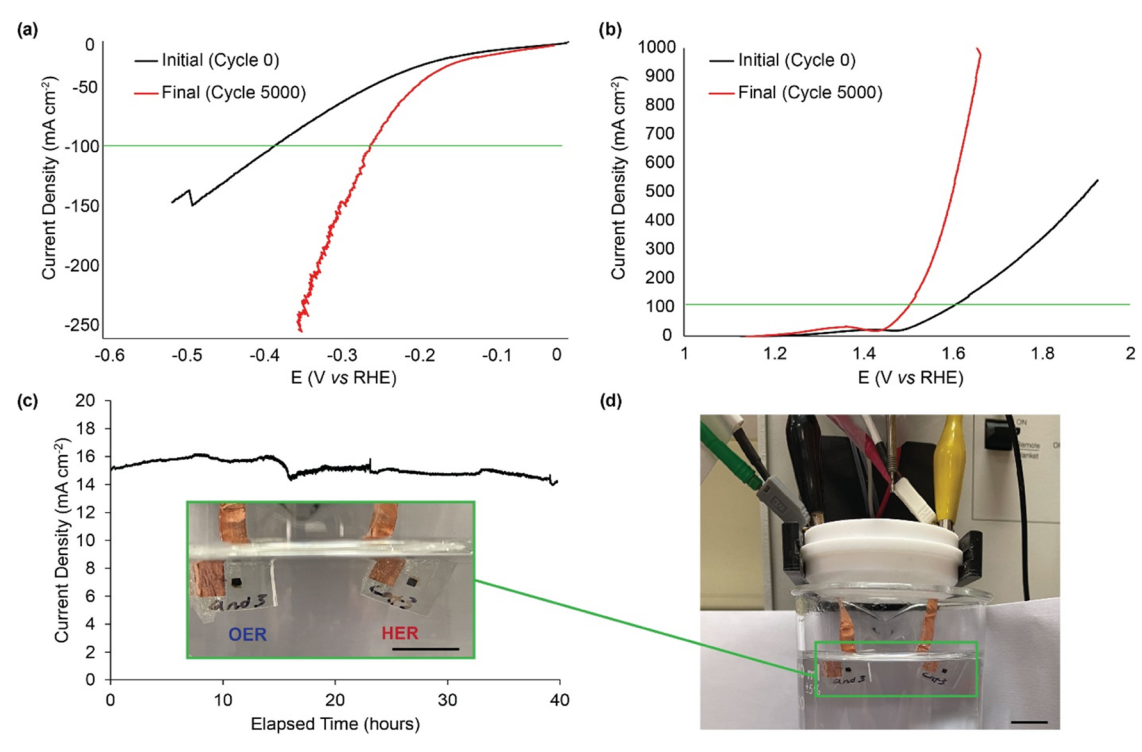


Figure 5. Overall water splitting stability of catalyst 1. (a) HER polarization curves for the initial LSV measurement (black) before cycling and the final LSV measurement after 5000 cycles (red). The overpotentials of the initial and final polarization curves are 404 and 263 mV at 100 mA cm⁻², respectively, compared to the 210 mV of the nonstability-tested catalyst (Figure 2c). (b) OER polarization curves for the initial LSV measurement (black) before cycling and the final LSV measurement after 5000 cycles (red). The overpotentials of the initial and final polarization curves are 370 and 272 mV at 100 mA cm⁻², respectively, compared to the 322 mV of the non-stability-tested catalyst (Figure 2d). Both LSV plots show that catalyst 1 is activated for performance by cycling and the performance gets better from the initial to the final polarization curves. The final overall ΔV at 100 mA cm⁻² is 1.77 V using the HER and OER overpotentials, which is similar to the 1.76 ± 0.01 V during the nonstability catalyst testing (Table S5). Due to the ΔV of both the stability and the nonstability testing catalyst falling within the standard deviation, and that nonstability testing also starts with cycling for ECSA (~60 cycles) before three runs of LSV testing before recording the overpotential, ΔV, and Tafel slope measurements, we believe that the catalyst is activated within that testing frame. We also see that from 1000 to 5000 cycles for both HER and OER that the CV plots are similar to each other, also corroborating the activation and stability (Figure S15a,b). (c) Chronoamperometry in a two-electrode system at 1.636 V with both cathode and anode as catalyst 1 demonstrated stability at 14–15 mA cm⁻² for 40 h. The constant potential was chosen based on the initial LSV of the two-probe system from 1 to 2 V where the current density was measured to be 20 mA cm⁻² (Figure S15c). Inset shows the electrode set up from (d). The large picture (d) shows the chronoamperometry setup. H₂ and O₂ production is seen during

This increase was indeed much smaller than the decrease from 0.71 to 0.54 that occurred when changing the structure of (Fe,Co,Ni)OOH from its catalytically active β -phase to its less active (more oxyphilic) h-phase.

Based on this result and using the Nørskov model (whereby the activation barrier for the rate-limiting OER/HER step is proportional to the largest of the energy differences between the reaction intermediates), the reaction OH* \rightarrow O* + H⁺ + e⁻ was found to be the rate-limiting step (Figure 4b). The overpotential was thus estimated as $\eta_{\text{OER}} = \Phi - \Phi_{\text{OER}} = [(\gamma - 1) \Delta E(\text{OH*}) + \delta]/e - \Phi_{\text{OER}}$, where Φ denotes the applied potential, $\Phi_{\text{OER}} = 1.23$ V vs RHE (reversible hydrogen electrode) is the equilibrium OER potential, $\gamma = 0.76$ is the calculated slope of the scaling relationships for β -(Cr,Fe,Co,Ni)OOH, and the composition-dependent offset δ captures model uncertainties in the multimetal configuration of the most active sites.

Once calibrated against the experimental overpotential of the Fe_{0.53}Co_{0.26}Ni_{0.20}O_x/C_y catalyst (with $\eta_{\rm OER}\approx 300$ mV, corresponding to $\delta_{\rm OER}\approx 1.21$ eV, and $\eta_{\rm HER}\approx 250$ mV, corresponding to $\delta_{\rm HER}\approx -0.07$ eV), this simple model enables us to predict the influence of Cr substitution on the HER and OER overpotentials of β -(Cr,Fe,Co,Ni)OOH. As shown in

Figure 4c, the overpotential was predicted to decrease by \sim 20 meV (corresponding to a 2-fold increase in the catalytic current) when adding one Cr cation at the bottom neighbor site [Cr_(below)], while increasing by 35–40 meV (corresponding to 4- to 5-fold decrease in catalytic activity) when one Cr cation was placed in the vicinity of the Ni site [Cr_(on-top)] or two Cr cations were surrounding the Ni site [Cr_(below) and Cr_(on-top)]. The same trend was found for the majority-spin dband center of the Ni cation (Figure 4c), whereby placing Cr at the bottom position [Cr_(below)] pushed up the d-band center closer to the Fermi level by 0.12 eV. We ascribe this effect to the depletion of the antibonding orbitals between the O or OH adsorbates and the eta-(Cr,Fe,Co,Ni)OOH surface.⁶³ In contrast, a reversal of the trend was observed with additional Cr, corresponding to a downshift of 0.3–0.4 eV in the d-bands. To confirm these results and assess the influence of the aqueous solvent on the predicted HER/OER trends, we applied the self-consistent continuum solvation model (SCCS) to our surface calculations. Using this model, we found a moderate decrease in the slope of the scaling relation from γ = 0.76 without solvent to $\gamma = 0.70$ with solvation (Figure S14). This slight decrease (of less than 10%) does not qualitatively affect the predictions of the model. These results, which are

summarized in Table S7, indicate that small amounts of Cr can significantly influence HER/OER and suggest that the activity of multimetal electrocatalysts can be effectively tuned *via* subsurface Cr substitution.

To explore whether catalyst 1 could be utilized for fuel cell application purposes as bifunctional water splitting catalysts, we tested its selectivity for HER and OER, its stability during the water splitting half-reactions, and its performance in a 2probe fuel cell system. To test catalyst 1's selectivity, we used an oxygen reduction reaction (ORR) activation experiment where we saw the catalyst was not active for ORR (Figure S15). This means the catalyst is selective for the HER and OER reactions, and that it will not significantly reduce the oxygen it produces during OER and convert it back to its hydroxyl reactants during ORR. We also cycled two catalyst 1 samples for 5000 cycles of HER and OER (Figure S16a,b) to determine the catalysts' stability. Cycle 0 is different than the rest of the reported measurements in this work as it is before any cycling or LSV and, thus, before the material is activated. The rest of the cycles (cycles 1000-5000) show stability. From cycle 0 to cycle 5000, activating the catalyst showed that the performance of HER and OER both improved by 39 and 98 mV, respectively (Figure 5a,b). The shift in oxidation states in the Cr, Co, and Ni sites as shown by XPS before and after catalytic testing (Figures S11 and S12) could explain the shift to an activated catalyst. The ΔV calculated from the final (cycle 5000) LSV overpotentials at 100 mA cm⁻² was 1.77 V, compared to the 60× ECSA-cycled and 4 LSV-cycled catalyst 1 ΔV of 1.76 \pm 0.01 V at 100 mA cm⁻². As the ΔV from the stability testing is within the standard deviation of ΔV in the 60× ECSA cycled and 4 LSV cycled catalyst 1 testing, we believe that the catalyst is properly activated before for all reported measurements in this work. LSV was first performed to find the potential reading at a current density of 20 mA cm⁻² to use for the application experiment (Figure S16c). Applying this constant potential, the 2-electrode system stabilized at 14-15 mA cm⁻² at a constant voltage of 1.636 V applied for 40 h with no significant loss in current density indicating the stability of the system in Figure 5c. Steady production of O₂ and H₂ products is seen in Video S1. During the two-electrode, single-chamber experiment, holding the current density at 100 mA cm⁻², catalyst 1 is stable for 5 h (Figure S17). However, we noticed that this instability was not due to the deactivation of the active sites, but instead due to the rapid bubble formation that caused damage to the catalyst itself, as we saw pieces of the catalyst delaminate from the substrate. This is an engineering challenge we would need to address in future work.

CONCLUSIONS

In this paper, we have demonstrated the ability of the LITV method for synthesizing a broad range of mixed metal catalysts for bifunctional HER and OER water splitting applications. The complex heterogeneous structure of the best quaternary metal catalysts resulting from the LITV synthesis, $Cr_{0.01}Fe_{0.27}Co_{0.34}Ni_{0.38}O_x/C_y$, contained nanocrystalline particles with high localization of Fe, Co, and Ni surrounded by an amorphous Fe and Cr oxide matrix. By doping a Fe, Co, and Ni catalyst with a small amount of Cr, the HER and OER performance was significantly increased due to better binding affinities according to DFT PDOS computations. The interface between the amorphous and crystalline phases was determined to be important by the annealing experiments, wherein as Fe

and Co oxides became more crystalline with increased annealing temperatures, HER performance worsened. Our best bifunctional catalyst was shown to be stable at 14–15 mA cm⁻² for at least 40 h in an electrolysis fuel cell setup demonstrating its potential application. In conclusion, LITV synthesis has proven to be a facile method for creating complex, heterogeneous, and bifunctional HER and OER catalysts and affecting their chemical and structural variables to enable a systemic understanding of catalytic mechanisms and optimized performance. The next steps may include scaling up synthesis processes for these complex, non-precious-multimetal catalysts and increasing the efficiency of the electrolytic fuel cell itself.

METHODS

Materials. All chemicals are commercially available and used as received. Iron(III) nitrate nonahydrate (98.0%, Alfa Aesar), chromium(III) nitrate nonahydrate (98.5%, Alfa Aesar), nickel(II) nitrate hexahydrate (98%, Alfa Aesar), cobalt(II) nitrate hexahydrate (98%, Fisher Scientific), phosphotungstic acid (83.51%, Chem-Impex Int'l, Inc.), ammonium molybdate (para) tetrahydrate (99%, Alfa Aesar), vanadium(IV) sulfate oxide hydrate (99.9%, Alfa Aesar), titanium(IV) oxysulfate-sulfuric acid hydrate (synthesis grade, Aldrich), copper(II) nitrate trihydrate (99%, Acros Organics), manganese(II) nitrate tetrahydrate (98%, Alfa Aesar), zinc nitrate hexahydrate (99%, Sigma-Aldrich), potassium hydroxide pellets (EMD). All metal and metal oxide precursor solutions were prepared by dissolving the precursor salts in ethylene glycol (99.8%, Alfa Aesar) at 1 M concentrations. Ternary and quaternary ratio precursor solutions were made by mixing different volumes of the 1 M solutions. Samples were deposited on fluorine-doped tin oxide glass substrate (FTO, TEC 15) 10 mm × 10 mm × 1.1 mm, R: 15 ohm/sq (MSE Supplies). Electrodes used for linear and cyclic voltammetry were a graphite auxiliary electrode (BASI) or a Pt auxiliary electrode (BASI) as the counter electrode and an Ag/AgCl reference electrode (BASI). Electrochemical testing was carried out in a 5–15 mL cell vial (BASI) with a Teflon cell top (BASI).

Direct Laser Writing Optical Setup. All depositions employed a Coherent Verdi G-series continuous wave laser operating at 532 nm. An output power of 2 W was directed through mirrors, a galvo scanner, and lenses to focus on the substrate with the fluid precursor for deposition. Lenses were used to collimate and expand the beam to fill the back of the microscope objective. The laser focus was translated using a galvo scanner (Nutfield open frame head XLR8-10 mm clear aperture), which allowed oscillation of the laser spot as it entered a microscope objective (High-Power Microspot Focusing air 50x Thorlabs objective with correction collar, 495–570 nm, with 0.60 NA) situated on an inverted microscope (ASI automated RAMM/modular infinity microscope system with motorized stage). Laser powers reported in the Material Deposition section were measured after the objective was 850 mW for all catalysts in this paper. A full schematic of the optical setup is described in Figure S1.

Material Deposition. The laser was focused through a microscope objective onto the substrate with the precursor solution to create the laser-induced thermal voxel, thereby depositing material directly from the precursor fluid without the need of an optical initiating absorber. A droplet of the mixed precursor solution was placed onto the FTO glass substrate, and a continuous wave 532 nm laser was focused with a 50×, 0.60 NA objective lens onto the interface between the precursor solution and the substrate. A laser power of 850 mW as measured after the objective was used for all catalyst depositions. Patterns were "drawn" with the laser by both scanning the laser with the galvo mirrors and translating the microscope stage. Specifically, catalysts were patterned by translating the microscope stage at 15 μ m s⁻¹ in the x and y directions in a snaking pattern with a laser scan rate of 500 μ m s⁻¹ and amplitude of 60 μ m back and forth in the y direction using the galvo mirrors. A 1 \times 1 mm² area was deposited for catalyst testing, then rinsed with 20 μ L

of deionized water, $3\times 20~\mu L$ of 1 M potassium hydroxide aqueous solution, and another 20 μL of deionized water The catalyst was then air-dried before characterization.

Characterization. *Profilometry.* Optical profilometry was performed using a Sensofar Metrology S lynx compact 3D optimal profiler. For profiling the catalyst, the focus would scan from below the substrate to above the catalyst to obtain the full profile. Surface area was calculated by using the width, length, and average height of the catalysts as measured by the instrument.

X-ray Diffraction (XRD). XRD was performed using a PANalytical Empyrean II with a Co source, a θ - θ goniometer, parallel beam optics, point focus in reflection mode, with an Xcelerator PASS detector and Fe β -filter operating at a step size of 0.03° s⁻¹ from 20 to 120° 2 θ using an XYZ stage.

Scanning Electron Microscopy (SEM) and Energy-Dispersity X-ray Spectroscopy (EDS). SEM images and EDS maps were taken on an FEI Nova NanoSEM 630 SEM with an accelerating voltage of 3 keV for imaging and 15 keV for EDS. Samples for SEM analysis were coated with a 5 nm layer of iridium metal to prevent charge build-up. EDS analysis has a sample penetration depth of 2 μ m and an error of \pm 5%. To calculate the output fraction atom % of the transition metals using EDS analysis, the atom % sum of the transition metals in a catalyst sample was used to divide the individual atom %. For example, in a MnFeCoNi sample, the total EDS analysis would yield the elements and atom % of C (31.32 atom %), O (49.03 atom %), Al (0.11 atom %), Si (0.09 atom %), Mn (2.78 atom %), Fe (12.64 atom %), Co (1.95 atom %), and Ni (2.09 atom %) for a total 100 atom %. To calculate the output fraction of an individual transition metal (TM), e.g., Fe in this sample, the equation would be

$$\frac{\text{individual TM atom \%}}{\text{sum TM atom \%}} = [12.64 \text{ atom \% (Fe})]$$

$$/[12.64 \text{ atom \% (Fe}) + 1.95 \text{ atom \% (Co}) + 2.09 \text{ atom \%}$$

$$(\text{Ni}) + 2.78 \text{ atom \% (Mn)}] = 0.65 \text{ for Fe}$$

Transmission Electron Microscopy (TEM). Particles of the laser-deposited samples were scratched off the FTO glass substrate surface, dispersed in ethanol, and ultrasonicated for 30 s. The particle dispersion was then drop-cast onto a lacey carbon TEM grid with copper support. HRTEM and STEM-EDS of the sample were performed using an FEI Talos F200X microscope at Penn State operating at an accelerating voltage of 200 kV, offering angstrom image resolution. A high-angle annular dark field (HAADF) detector was used for STEM image acquisition and EDS data collection using the Super-X EDS quad detector system at an accelerating voltage of 200 kV and current of ~0.15 nA. Standardless Cliff-Lorimer quantification was performed on the deconvoluted EDS line intensity data using the Bruker Espirit software.

X-ray Photoelectron Spectroscopy (XPS). XPS measurements were performed using a Physical Electronics PHI VersaProbe III equipped with a concentric hemispherical analyzer. Samples were pumped to pressures of $\sim 10^{-10}$ Torr and irradiated using a monochromatic Al K α X-ray source (15 kV, ~ 48 W) over a spot size of 200 μ m. The survey and high-resolution spectra were recorded with pass energies of 280 and 55 eV, with step sizes of 1 and 0.2 eV, respectively. Charge neutralizers (low-energy electrons and argon ions) were used during all acquisitions. All survey spectra were charge referenced with respect to the adventitious carbon peak at 284.8 eV. 64,65

For the depth profile, the sample was etched/sputtered using an Ar⁺ ion beam with an energy of 4 kV scanned over a 2 mm \times 2 mm area. Sputter time intervals were 10 min, and sputtering was carried out for a total of 70 min. These conditions correspond to an etch rate of \sim 20 nm min⁻¹ for SiO₂ on Si substrate. The exact etch rate of the samples analyzed is not known due to the absence of a reference and the roughness of the sample. However, it is assumed that the etch rate of the analyzed samples are lower than that of SiO₂ based on metal oxide samples studied. Depth profile spectra were recorded using a pass energy of 112 eV with a step size of 0.2 eV.

All XPS data were analyzed with CasaXPS Version 2.3.23.PR1.0.⁶⁶ All peaks except for nickel were fitted using an Iterated Shirley background subtraction using a symmetric Lorentzian lineshape LF (1,1,255,380,5). $^{64-66}$ Ni peaks were fitted using a default background subtraction using the same LF lineshape as the others. Peaks were fitted using binding energy and full width at half-maximum (FWHM) values obtained from databases and relevant literature. $^{57-60,64-66}$ XPS data analysis has a penetration depth of 30 nm and an error of 10%. Uncertainties in background subtraction and peak fittings were all calculated using a Monte Carlo approach in CasaXPS. 39,66

Electrochemical Characterization. LSV, CV, and EIS were performed on a three-electrode configuration using a Versa STAT 4 potentiostat. A 1 M KOH solution was used as electrolyte. The asdeposited catalyst samples on FTO (15 Ω Sq⁻¹) were directly used as the working electrode, a graphite auxiliary electrode or a Pt RDE auxiliary electrode as the counter electrode, and a saturated Ag/AgCl electrode as the reference electrode. When using the Pt RDE auxiliary electrode, we found that in some instances after catalytic testing, there was a very small amount Pt dissolution (0.27 atom %) onto one unreported catalyst. While no evidence of Pt dissolution and lowered HER overpotentials due to Pt activity were seen on the other catalysts reported in this manuscript, all of the catalysts reported in the main text were measured with a graphite counter electrode. All of the catalysts that were tested with the Pt counter electrode in the Supporting Information are labeled, and these catalysts were either unstable or did not have efficient performances.

EIS was performed at 0 mV overpotential on the frequency range from 0.1 Hz to 1 MHz. ECSA was determined by measuring the capacitive current associated with double-layer charging as a function of scan rate in CV. The potential window for CV had a width of 1.0 V and the scan rates were 10, 20, 30, 40, 50, 60, 70, 80, 90, and 100 mV s⁻¹. There is a minimum of 60 cycles in the ECSA measurement. The double-layer capacitance (C_{dl}) was estimated by plotting the Δj at the middle point of the potential window against the scan rate. The slope is twice the $C_{\rm dl}$, which is proportional to the ECSA. Linear sweep voltammetry (LSV) was performed with iR-compensation at a scan rate of 5 mV s⁻¹, from -1 to -1.6 V (vs Ag/AgCl) for HER and from 0 to 1 V (vs Ag/AgCl) for OER. To stabilize the electrode surface, the electrode was cycled three times before data collection. The ΔV value was calculated by adding the absolute values of the HER and OER overpotentials to the minimal theoretical voltage required for overall water splitting (1.23 V).

For cycling performance measurements, after stabilizing the electrode surface, an initial LSV was performed at a scan rate of 5 mV s $^{-1}$ from -1 to -1.6 V (vs Ag/AgCl) for HER or from 0 to 1 V (vs Ag/AgCl) for OER. Then, the sample was subjected to 5000 cycles of cyclic voltammetry at a scan rate of 100 mV s $^{-1}$. The window for CV was from 0.2 to 0.5 V (vs Ag/AgCl) for the case of OER cycling, or from -1.1 to -1.4 V (vs Ag/AgCl) for HER cycling. Finally, a post-cycling LSV measurement was recorded using the same parameters used for the initial measurement.

To test the selectivity of the catalyst for HER and OER we tested for ORR. For this, a 0.1 M KOH solution was purged with $\rm N_2$ for 30 min and used as electrolyte to run CV for 20 cycles in a window between 0.2 and $\rm -0.8~V~(vs~Ag/AgCl)$ with a scan rate of 50 mV s⁻¹. Then, the electrolyte was changed for a 0.1 M KOH solution that had been purged with $\rm O_2$ for 30 min, and the cyclic voltammetry was repeated while $\rm O_2$ was continually bubbled into the electrolyte. Any $\rm O_2$ reduction would have been recorded as additional peaks present during the $\rm O_2$ CV compared to the baseline of the $\rm N_2$ CV.

For the testing of catalyst durability in an application setup, two catalysts made with catalyst 1 synthesis parameters were used as the anode and cathode on a two-electrode cell configuration. LSV with a scan rate of 5 mV s $^{-1}$ from 1 to 2 V was used to determine the potential required to record a current density of 20 or 100 mA cm $^{-2}$, which was found to be 1.636 V at 20 mA cm $^{-2}$ and 2.15 V at 100 mA cm $^{-2}$ respectively. That potential was then held constant for 40 h in a chronoamperometry experiment using the 2-electrode cell system or until performance stopped to study the stability of an electrolytic cell for fuel production using water electrolysis. A final LSV measurement is recorded after the 40-h chronoamperometry using the same parameters used for the initial measurement.

First-Principles Calculations. Self-consistent electronic-structure calculations of β -(Fe,Co,Ni)OOH surfaces with increasing amounts of Cr were performed using dispersion-corrected semilocal (Perdew-Burke–Ernzerhof) density functional theory with collinear spin polarization. The semiempirical DFT-D2^{67,68} dispersion correction was applied. Ionic cores were described using the projectoraugmented wave method implemented in the plane-wave Quantum-ESPRESSO code.⁶⁹ Each structure was relaxed using a 680 eV energy cutoff and a Monkhorst-Pack grid of $4 \times 2 \times 1$ k-points to sample the Brillouin zone with convergence criteria on the total energy of 1 meV/atom. The systems were modeled in their antiferromagnetic states. The positions of the surface and subsurface atoms were allowed to relax during geometric optimization while the remaining atoms were fixed. The Brillouin-zone integrals were performed using the Marzari-Vanderbilt cold smearing method, where we used a smearing width of 0.01 eV.70 The projected density of states (PDOS) was calculated using tetrahedral interpolation.

Turnover Frequency (TOF) Equations (Eqs 2–4) for Determining Intrinsic HER and OER Electrocatalytic Activity. TOF was estimated based on the assumption that all of the 3d metal atoms (Cr, Fe, Co, and Ni) are considered as active sites. Metal concentration was obtained by the XPS depth profile survey spectra shown in Figure S7. The total weight of the catalyst is \sim 0.1 mg, which was calculated by taking the weight of a powdered 3 \times 3 mm² sample (0.00075 g) and dividing by 9 (as a 3 \times 3 mm square is \sim 9 \times the size of a 1 \times 1 mm square). The area of the catalyst is \sim 0.01 cm².

$$TOF = \frac{total \ oxygen \ turnovers \ per \ geometric \ area}{the \ number \ of \ metal \ active \ sites} \tag{2}$$

number of metal active sites

=
$$\sum$$
 [metal loading on the electrode (g cm⁻²)
× metal concentration (wt %) × 6.022 × 10²³ mol⁻¹]
/[metal atomic weight (g mol⁻¹)] (3)

total oxygen turnovers

= |J mA cm⁻²| ×
$$\left(\frac{1 \text{ C s}^{-1}}{1000 \text{ mA}}\right)$$
 × $\left(\frac{1 \text{ mol}^{-1}}{96 \text{ 485.3 C}}\right)$ × $\left(\frac{1 \text{ mol}}{4 \text{ mol}^{-1}}\right)$
× $\left(\frac{6.022 \times 10^{23} \text{ molecules O}_2}{1 \text{ mol O}_2}\right)$ (4)

For example, the best-performing sample catalyst 1, when the overpotential is 350 mV, j is 1450 mA cm⁻².

number of total metal active sites = total metals (mol cm⁻²)
×
$$(6.022 \times 10^{23} \text{ mol}^{-1}) = 0.000174 \times (6.022 \times 10^{23} \text{ mol}^{-1})$$

= $1.05 \times 10^{20} \text{ cm}^{-2}$

total oxygen turnovers

= |1450 mA cm⁻²| ×
$$\left(\frac{1 \text{ C s}^{-1}}{1000 \text{ mA}}\right)$$
 × $\left(\frac{1 \text{ mol}^{-1}}{96 \text{ 485.3 C}}\right)$
× $\left(\frac{1 \text{ mol}}{4 \text{ mol}^{-1}}\right)$ × $\left(\frac{6.022 \times 10^{23} \text{ molecules O}_2}{1 \text{ mol O}_2}\right)$
= 2.26 × 10¹⁸ cm⁻² s⁻¹

TOF =
$$\frac{\text{total oxygen turnovers per geometric area}}{\text{the number of metal active sites per geometric area}}$$

= $\frac{2.26 \times 10^{18} \text{ cm}^{-2} \text{ s}^{-1}}{1.05 \times 10^{20} \text{ cm}^{-2}} = 0.0216 \text{ s}^{-1}$

ASSOCIATED CONTENT

Supporting Information

The Supporting Information is available free of charge at https://pubs.acs.org/doi/10.1021/acsaem.2c03973.

Electrochemical data, Raman, XRD, TEM, and EDS data, as well as additional details of the Monte Carlo and DFT structures and computations (Figures S1–S17); EDS and electrochemical performance data of the samples, and the predicted reaction energies and overpotentials for different phases and compositions of HER–OER catalysts (Tables S1–S7) (PDF)

 O_2 and H_2 production from two catalyst 1 samples as cathode and anode in a two-electrode HER-OER setup (Video S1) (MP4)

AUTHOR INFORMATION

Corresponding Authors

Mauricio Terrones — Department of Chemistry, The Pennsylvania State University, University Park, Pennsylvania 16802, United States; Department of Materials Science and Engineering, Department of Physics, Center for Atomically Thin Multifunctional Coatings, and Center for 2-Dimensional and Layered Materials, The Pennsylvania State University, University Park, Pennsylvania 16802, United States; Research Initiative for Supra-Materials, Shinshu University, Nagano 380-8553, Japan; orcid.org/0000-0003-0010-2851; Email: mut11@psu.edu

Lauren D. Zarzar — Department of Chemistry, The Pennsylvania State University, University Park, Pennsylvania 16802, United States; Department of Materials Science and Engineering and Materials Research Institute, The Pennsylvania State University, University Park, Pennsylvania 16802, United States; orcid.org/0000-0002-3287-3602; Email: ldz4@psu.edu

Authors

Shannon McGee – Department of Chemistry, The Pennsylvania State University, University Park, Pennsylvania 16802, United States

Andres Fest – Department of Materials Science and Engineering, The Pennsylvania State University, University Park, Pennsylvania 16802, United States

Cierra Chandler – Department of Materials Science and Engineering, The Pennsylvania State University, University Park, Pennsylvania 16802, United States

Nabila N. Nova – Department of Chemistry, The Pennsylvania State University, University Park, Pennsylvania 16802, United States

Yu Lei — Department of Physics, Center for Atomically Thin Multifunctional Coatings, and Center for 2-Dimensional and Layered Materials, The Pennsylvania State University, University Park, Pennsylvania 16802, United States; Institute of Materials Research & Center of Double Helix, Tsinghua Shenzhen International Graduate School, Tsinghua University, Shenzhen 518055, China; orcid.org/0000-0003-4693-7408

James Goff – Department of Materials Science and Engineering, The Pennsylvania State University, University Park, Pennsylvania 16802, United States; ⊚ orcid.org/ 0000-0001-7026-7200

Susan B. Sinnott – Department of Chemistry, The Pennsylvania State University, University Park, Pennsylvania 16802, United States; Department of Materials Science and Engineering, Materials Research Institute, and Penn State Institutes of Energy and the Environment, The Pennsylvania State University, University Park, Pennsylvania 16802, United States

Ismaila Dabo — Department of Materials Science and Engineering, Materials Research Institute, and Penn State Institutes of Energy and the Environment, The Pennsylvania State University, University Park, Pennsylvania 16802, United States; orcid.org/0000-0003-0742-030X

Complete contact information is available at: https://pubs.acs.org/10.1021/acsaem.2c03973

Notes

The authors declare no competing financial interest.

ACKNOWLEDGMENTS

S.M., A.F., Y.L., L.D.Z., and M.T. thank the Institutes of Energy and the Environment seed grant program at Penn State, S.M. and L.D.Z. thank the Packard Foundation through support from the Packard Fellowship for Science and Engineering (Grant 2019-69664) and the NSF (Grant CMMI-2046819). N.N.N. and L.D.Z. thank the Sloan Foundation (FG-2020-12707). C.C., J.G., S.B.S., and I.D. acknowledge financial support from the U.S. Department of Energy, Office of Science, Basic Energy Sciences, CPIMS Program, under Award No. DE-SC0018646. N.N.N. acknowledges financial support from the National Science Foundation Materials Research Science and Engineering Center for Nanoscale Science at Penn State University under grants NSF-DMR-2011839 and NSF-DMR 1420620. Y.L. acknowledges the Scientific Research Start-up Funds (no. QD2021033C) at Tsinghua Shenzhen International Graduate School.

REFERENCES

- (1) Ritchie, H.; Roser, M. Energy. https://ourworldindata.org/energy (accessed October 03, 2022).
- (2) Siracusano, S.; Hodnik, N.; Jovanovic, P.; Ruiz-Zepeda, F.; Šala, M.; Baglio, V.; Aricò, A. S. New Insights into the Stability of a High Performance Nanostructured Catalyst for Sustainable Water Electrolysis. *Nano Energy* **2017**, *40*, 618–632.
- (3) Khan, M. A.; Zhao, H.; Zou, W.; Chen, Z.; Cao, W.; Fang, J.; Xu, J.; Zhang, L.; Zhang, J. Recent Progresses in Electrocatalysts for Water Electrolysis. *Electrochem. Energy Rev.* **2018**, *1*, 483–530.
- (4) Li, D.; Chen, X.; Lv, Y.; Zhang, G.; Huang, Y.; Liu, W.; Li, Y.; Chen, R.; Nuckolls, C.; Ni, H. An Effective Hybrid Electrocatalyst for the Alkaline HER: Highly Dispersed Pt Sites Immobilized by a Functionalized NiRu-Hydroxide. *Appl. Catal., B* **2020**, 269, No. 118824.
- (5) Lee, Y.; Suntivich, J.; May, K. J.; Perry, E. E.; Shao-Horn, Y. Synthesis and Activities of Rutile IrO₂ and RuO₂ Nanoparticles for Oxygen Evolution in Acid and Alkaline Solutions. *J. Phys. Chem. Lett.* **2012**, *3*, 399–404.
- (6) Kim, J. S.; Kim, B.; Kim, H.; Kang, K. Recent Progress on Multimetal Oxide Catalysts for the Oxygen Evolution Reaction. *Adv. Energy Mater.* **2018**, *8*, 1702774.
- (7) Zeng, K.; Zhang, D. Recent Progress in Alkaline Water Electrolysis for Hydrogen Production and Applications. *Prog. Energy Combust. Sci.* **2010**, *36*, 307–326.
- (8) Sanath, Y.; De Silva, K.; Middleton, P. H.; Kolhe, M. Performance Analysis of Single Cell Alkaline Electrolyser Using Mathematical Model. *IOP Conf. Ser. Mater. Sci. Eng.* **2019**, 605, No. 012002.

- (9) Parra-Puerto, A.; Ng, K. L.; Fahy, K.; Goode, A. E.; Ryan, M. P.; Kucernak, A. Supported Transition Metal Phosphides: Activity Survey for HER, ORR, OER, and Corrosion Resistance in Acid and Alkaline Electrolytes. *ACS Catal.* **2019**, *9*, 11515–11529.
- (10) Durst, J.; Simon, C.; Siebel, A.; Rheinlander, P.; Schuler, T.; Hanzlik, M.; Herranz, J.; Hasche, F.; Gasteiger, H. A. Hydrogen Oxidation and Evolution Reaction (HOR/HER) on Pt Electrodes in Acid vs. Alkaline Electrolytes: Mechanism, Activity and Particle Size Effects. ECS Trans. 2014, 64, 1069–1080.
- (11) Labata, M. F.; Li, G.; Ocon, J.; Chuang, P. Y. A. Insights on Platinum-Carbon Catalyst Degradation Mechanism for Oxygen Reduction Reaction in Acidic and Alkaline Media. *J. Power Sources* **2021**, 487, No. 229356.
- (12) Batchelor, T. A. A.; Pedersen, J. K.; Winther, S. H.; Castelli, I. E.; Jacobsen, K. W.; Rossmeisl, J. High-Entropy Alloys as a Discovery Platform for Electrocatalysis. *Joule* **2019**, *3*, 834–845.
- (13) You, B.; Tang, M. T.; Tsai, C.; Abild-Pedersen, F.; Zheng, X.; Li, H. Enhancing Electrocatalytic Water Splitting by Strain Engineering. *Adv. Mater.* **2019**, *31*, No. 1807001.
- (14) Tomboc, G. M.; Kwon, T.; Joo, J.; Lee, K. High Entropy Alloy Electrocatalysts: A Critical Assessment of Fabrication and Performance. J. Mater. Chem. A 2020, 8, 14844–14862.
- (15) Li, H.; Zhu, H.; Zhang, S.; Zhang, N.; Du, M.; Chai, Y. Nano High-Entropy Materials: Synthesis Strategies and Catalytic Applications. *Small Struct.* **2020**, *1*, No. 2000033.
- (16) Yeh, J. W. Alloy Design Strategies and Future Trends in High-Entropy Alloys. *JOM* **2013**, *65*, 1759–1771.
- (17) Trasatti, S. Electrocatalysis by Oxides Attempt at a Unifying Approach. J. Electroanal. Chem. Interfacial Electrochem. 1980, 111, 125–131.
- (18) Xue, Z.; Zhang, X.; Qin, J.; Liu, R. Revealing Ni-Based Layered Double Hydroxides as High-Efficiency Electrocatalysts for the Oxygen Evolution Reaction: A DFT Study. *J. Mater. Chem. A* **2019**, *7*, 23091–23097.
- (19) Hona, R. K.; Karki, S. B.; Cao, T.; Mishra, R.; Sterbinsky, G. E.; Ramezanipour, F. Sustainable Oxide Electrocatalyst for Hydrogenand Oxygen- Evolution Reactions. *ACS Catal.* **2021**, *11*, 14605–14614.
- (20) Wu, A.; Xie, Y.; Ma, H.; Tian, C.; Gu, Y.; Yan, H.; Zhang, X.; Yang, G.; Fu, H. Integrating the Active OER and HER Components as the Heterostructures for the Efficient Overall Water Splitting. *Nano Energy* **2018**, *44*, 353–363.
- (21) Glasscott, M. W.; Pendergast, A. D.; Goines, S.; Bishop, A. R.; Hoang, A. T.; Renault, C.; Dick, J. E. Electrosynthesis of High-Entropy Metallic Glass Nanoparticles for Designer, Multi-Functional Electrocatalysis. *Nat. Commun.* **2019**, *10*, No. 2650.
- (22) Chen, J.; Ren, B.; Cui, H.; Wang, C. Constructing Pure Phase Tungsten-Based Bimetallic Carbide Nanosheet as an Efficient Bifunctional Electrocatalyst for Overall Water Splitting. *Small* **2020**, *16*, 1907556.
- (23) Yu, F.; Zhou, H.; Huang, Y.; Sun, J.; Qin, F.; Bao, J.; Goddard, W. A.; Chen, S.; Ren, Z. High-Performance Bifunctional Porous Non-Noble Metal Phosphide Catalyst for Overall Water Splitting. *Nat. Commun.* **2018**, *9*, No. 2551.
- (24) Liu, X.; You, B.; Sun, Y. Facile Surface Modification of Ubiquitous Stainless Steel Led to Competent Electrocatalysts for Overall Water Splitting. ACS Sustainable Chem. Eng. 2017, 5, 4778–4784.
- (25) Kindle, C.; Castonguay, A.; McGee, S.; Tomko, J.; Hopkins, P.; Zarzar, L. Direct Laser Writing from Aqueous Precursors for Nano to Microscale Topographical Control, Integration, and Synthesis of Nanocrystalline Mixed Metal Oxides. *ACS Appl. Nano Mater.* **2019**, *2*, 2581–2586.
- (26) Zarzar, L. D.; Swartzentruber, B. S.; Donovan, B. F.; Hopkins, P. E.; Kaehr, B. Using Laser-Induced Thermal Voxels to Pattern Diverse Materials at the Solid-Liquid Interface. *ACS Appl. Mater. Interfaces* **2016**, *8*, 21134–21139.
- (27) McGee, S.; Lei, Y.; Goff, J.; Wilkinson, C. J.; Nova, N. N.; Kindle, C. M.; Zhang, F.; Fujisawa, K.; Dimitrov, E.; Sinnott, S. B.;

- Dabo, I.; Terrones, M.; Zarzar, L. Single-Step Direct Laser Writing of Multimetal Oxygen Evolution Catalysts from Liquid Precursors. *ACS Nano* **2021**, *15*, 9796–9807.
- (28) Nova, N. N.; Zarzar, L. D. Direct Laser Writing of Graphitic Carbon from Liquid Precursors. *Chem. Mater.* **2022**, 34, 4602–4612.
- (29) Zarzar, L. D.; Swartzentruber, B. S.; Harper, J. C.; Dunphy, D. R.; Brinker, C. J.; Aizenberg, J.; Kaehr, B. Multiphoton Lithography of Nanocrystalline Platinum and Palladium for Site-Specific Catalysis in 3D Microenvironments. *J. Am. Chem. Soc.* **2012**, *134*, 4007–4010.
- (30) Castonguay, A. C.; Yi, N.; Li, B.; Zhao, J.; Li, H.; Gao, Y.; Nova, N. N.; Tiwari, N.; Zarzar, L. D.; Cheng, H. Direct Laser Writing of Microscale Metal Oxide Gas Sensors from Liquid Precursors. *ACS Appl. Mater. Interfaces* **2022**, *14*, 28163–28173.
- (31) Xu, D.; Stevens, M. B.; Rui, Y.; DeLuca, G.; Boettcher, S. W.; Reichmanis, E.; Li, Y.; Zhang, Q.; Wang, H. The Role of Cr Doping in Ni–Fe Oxide/(Oxy)Hydroxide Electrocatalysts for Oxygen Evolution. *Electrochim. Acta* **2018**, 265, 10–18.
- (32) Xiong, J.; Li, J.; Shi, J.; Zhang, X.; Suen, N. T.; Liu, Z.; Huang, Y.; Xu, G.; Cai, W.; Lei, X.; Feng, L.; Yang, Z.; Huang, L.; Cheng, H. *In Situ* Engineering of Double-Phase Interface in Mo/Mo₂C Heteronanosheets for Boosted Hydrogen Evolution Reaction. *ACS Energy Lett.* **2018**, *3*, 341–348.
- (33) Chen, W.; Pei, J.; He, C. T.; Wan, J.; Ren, H.; Wang, Y.; Dong, J.; Wu, K.; Cheong, W. C.; Mao, J.; Zheng, X.; Yan, W.; Zhuang, Z.; Chen, C.; Peng, Q.; Wang, D.; Li, Y. Single Tungsten Atoms Supported on MOF-Derived N-Doped Carbon for Robust Electrochemical Hydrogen Evolution. *Adv. Mater.* 2018, 30, No. 1800396.
- (34) Rosalbino, F.; Delsante, S.; Borzone, G.; Scavino, G. Electrocatalytic Activity of Crystalline Ni-Co-M (M = Cr, Mn, Cu) Alloys on the Oxygen Evolution Reaction in an Alkaline Environment. *Int. J. Hydrogen Energy* **2013**, *38*, 10170–10177.
- (35) Wyckoff, R. W. Crystal Structures, 2nd ed.; Interscience Publishers: New York, NY, 1963.
- (36) Wang, F.; Inoue, A.; Kong, F. L.; Han, Y.; Zhu, S. L.; Shalaan, E.; Al-Marouki, F. Formation, Thermal Stability and Mechanical Properties of High Entropy (Fe,Co,Ni,Cr,Mo)-B Amorphous Alloys. *J. Alloys Compd.* **2018**, 732, 637–645.
- (37) Plata-Torres, M.; Torres-Huerta, A. M.; Domínguez-Crespo, M. A.; Arce-Estrada, E. M.; Ramírez-Rodríguez, C. Electrochemical Performance of Crystalline Ni-Co-Mo-Fe Electrodes Obtained by Mechanical Alloying on the Oxygen Evolution Reaction. *Int. J. Hydrogen Energy* **2007**, 32, 4142–4152.
- (38) Carlton, R. A.; Lyman, C. E.; Roberts, J. E. Accuracy and Precision of Quantitative Energy-Dispersive X-Ray Spectrometry in the Environmental Scanning Electron Microscope. *Scanning* **2004**, *26*, 167–174.
- (39) Cumpson, P. J.; Seah, M. P. Random Uncertainties in AES and XPS: I: Uncertainties in Peak Energies, Intensities and Areas Derived from Peak Synthesis. *Surf. Interface Anal.* **1992**, *18*, 345–360.
- (40) Pikula, T.; Oleszak, D.; Pękała, M. Hyperfine Interactions and Some Magnetic Properties of Nanocrystalline Co₄₀Fe₅₀Ni₁₀ and Co₅₀Fe₄₅Ni₅ Alloys Prepared by Mechanical Synthesis and Subsequently Heat Treated. *Acta Phys. Pol. A* **2011**, *119*, 52–55.
- (41) Semen'ko, M.; Ostapenko, R.; Teselko, P.In Synthesis and Characterization of Nanocrystalline CrFeCoNi Alloy by High Energetic Mechanical Alloying, IEEE 7th International Conference Nanomaterials: Application & Properties (NAP), 2017; pp 7–10.
- (42) Ju, S.; Cai, T.-Y.; Lu, H.-S.; Gong, C.-D. Pressure-Induced Crystal Structure and Spin-State Transitions in Magnetite (Fe₃O₄). *J. Am. Chem. Soc.* **2012**, *134*, 13780–13786.
- (43) Prabaharan, D. D. M.; Sadaiyandi, K.; Mahendran, M.; Sagadevan, S. Precipitation Method and Characterization of Cobalt Oxide Nanoparticles. *Appl. Phys. A* **2017**, *123*, 264.
- (44) Gupta, A.; Kumar, A.; Hegde, M. S.; Waghmare, U. V. Structure of Ce_{1-x} Sn_xO₂ and Its Relation to Oxygen Storage Property from First-Principles Analysis. *J. Chem. Phys.* **2010**, *132*, No. 194702.
- (45) Jubb, A. M.; Allen, H. C. Vibrational Spectroscopic Characterization of Hematite, Maghemite, and Magnetite Thin Films Produced

- by Vapor Deposition. ACS Appl. Mater. Interfaces 2010, 2, 2804–2812.
- (46) Li, Y.; Qiu, W.; Qin, F.; Fang, H.; Hadjiev, V. G.; Litvinov, D.; Bao, J. Identification of Cobalt Oxides with Raman Scattering and Fourier Transform Infrared Spectroscopy. *J. Phys. Chem. C* **2016**, *120*, 4511–4516.
- (47) Namduri, H.; Nasrazadani, S. Quantitative Analysis of Iron Oxides Using Fourier Transform Infrared Spectrophotometry. *Corros. Sci.* **2008**, *50*, 2493–2497.
- (48) Luisetto, I.; Pepe, F.; Bemporad, E. Preparation and Characterization of Nano Cobalt Oxide. *J. Nanopart. Res.* **2008**, *10*, 59–67.
- (49) Alrehaily, L. M.; Joseph, J. M.; Musa, A. Y.; Guzonas, D. A.; Wren, J. C. Gamma-Radiation Induced Formation of Chromium Oxide Nanoparticles from Dissolved Dichromate. *Phys. Chem. Chem. Phys.* **2013**, *15*, 98–107.
- (50) Lefèvre, G. In Situ Fourier-Transform Infrared Spectroscopy Studies of Inorganic Ions Adsorption on Metal Oxides and Hydroxides. Adv. Colloid Interface Sci. 2004, 107, 109–123.
- (51) Sangeetha, S.; Basha, R.; Sreeram, K. J.; Sangilimuthu, S. N.; Unni Nair, B. Functional Pigments from Chromium(III) Oxide Nanoparticles. *Dyes Pigm.* **2012**, *94*, 548–552.
- (52) He, J.; Weekes, D. M.; Cheng, W.; Dettelbach, K. E.; Huang, A.; Li, T.; Berlinguette, C. P. Photodecomposition of Metal Nitrate and Chloride Compounds Yields Amorphous Metal Oxide Films. *J. Am. Chem. Soc.* **2017**, *139*, 18174–18177.
- (53) Devi, J.; Yadav, M.; Sharma, S.; Devi, J. Synthesis and Characterization of Co(II), Ni(II), Cu(II), and Zn(II) Complexes of Thiosemicarbazones. *J. Therm. Anal. Calorim.* **2018**, *10*, 1–6.
- (54) Wu, Z.; Wang, X.; Huang, J.; Gao, F. A Co-Doped Ni-Fe Mixed Oxide Mesoporous Nanosheet Array with Low Overpotential and High Stability towards Overall Water Splitting. *J. Mater. Chem. A* **2018**, *6*, 167–178.
- (55) Biesinger, M. C.; Payne, B. P.; Grosvenor, A. P.; Lau, L. W. M.; Gerson, A. R.; Smart, R. S. C. Resolving Surface Chemical States in XPS Analysis of First Row Transition Metals, Oxides and Hydroxides: Cr, Mn, Fe, Co and Ni. *Appl. Surf. Sci.* **2011**, *257*, 2717–2730.
- (56) Zhao, X.; Xue, Z.; Chen, W.; Wang, Y.; Mu, T. Eutectic Synthesis of High-Entropy Metal Phosphides for Electrocatalytic Water Splitting. *ChemSusChem* **2020**, *13*, 2038–2042.
- (57) Budi, S.; Kurniawan, B.; Mott, D. M.; Maenosono, S.; Umar, A. A.; Manaf, A. Comparative Trial of Saccharin-Added Electrolyte for Improving the Structure of an Electrodeposited Magnetic FeCoNi Thin Film. *Thin Solid Films* **2017**, *642*, 51–57.
- (58) López, M. C.; Ortiz, G. F.; Lavela, P.; Alcántara, R.; Tirado, J. L. Improved Energy Storage Solution Based on Hybrid Oxide Materials. ACS Sustainable Chem. Eng. 2013, 1, 46–56.
- (59) Li, Z.; Cai, L.; Song, M.; Shen, Y.; Wang, X.; Li, J.; Wang, J.; Wang, P.; Tian, L. Ternary FeCoNi Alloy Nanoparticles Embedded in N-Doped Carbon Nanotubes for Efficient Oxygen Evolution Reaction Electrocatalysis. *Electrochim. Acta* **2020**, *339*, No. 135886.
- (60) Bai, L.; Wen, X.; Guan, J. Amorphous FeCoNi Oxide for Oxygen Evolution Reaction. *Mater. Today Energy* **2019**, *12*, 311–317.
- (61) Fernández, E.; Moses, P. G.; Toftelund, A.; Hansen, H. A.; Martínez, J. I.; Abild-Pedersen, F.; Kleis, J.; Hinnemann, B.; Rossmeisl, J.; Bligaard, T.; Nørskov, J. K. Scaling Relationships for Adsorption Energies on Transition Metal Oxide, Sulfide, and Nitride Surfaces. *Angew. Chem., Int. Ed.* **2008**, *47*, 4683–4686.
- (62) Nørskov, J. K.; Rossmeisl, J.; Logadottir, A.; Lindqvist, L.; Kitchin, J. R.; Bligaard, T.; Jónsson, H. Origin of the Overpotential for Oxygen Reduction at a Fuel-Cell Cathode. *J. Phys. Chem. B* **2004**, *108*, 17886–17892.
- (63) Bhattacharjee, S.; Waghmare, U. V.; Lee, S. C. An Improved D-Band Model of the Catalytic Activity of Magnetic Transition Metal Surfaces. *Sci. Rep.* **2016**, *6*, No. 35916.
- (64) Briggs, D. X-Ray Photoelectron Spectroscopy (XPS), 2nd ed.; Eden Prairie: MN, 2005.
- (65) X-ray Photoelectron Spectroscopy Database, NIST, 2022.

- (66) Fairely, N. CasaXPS Manual 2.3. 15 Getting Started with CasaXPS, Casa Software Ltd., 2009.
- (67) Grimme, S. Semiempirical GGA-Type Density Functional Constructed with a Long-Range Dispersion Correction. *J. Comput. Chem.* **2006**, 27, 1787–1799.
- (68) Barone, V.; Casarin, M.; Forrer, D.; Pavone, M.; Sambi, M.; Vittadini, A. Role and Effective Treatment of Dispersive Forces in Materials: Polyethylen and Graphite Crystals as Test Cases. *J. Comput. Chem.* **2009**, *30*, 934–939.
- (69) Giannozzi, P.; Andreussi, O.; Brumme, T.; Bunau, O.; Nardelli, M. B.; Calandra, M.; Car, R.; Cavazzoni, C.; Ceresoli, D.; Cococcioni, M.; Colonna, N.; Carnimeo, I.; Dal Corso, A.; de Gironcoli, S.; Delugas, P.; DiStasio, R. A.; Ferretti, A.; Floris, A.; Fratesi, G.; Fugallow, G.; Gebauer, R.; Gerstmann, U.; Giustino, F.; Gorni, T.; Jia, J.; Kawamura, M.; Ko, H. Y.; Kokalj, A.; Küçükbenli, E.; Lazzeri, M.; Marsili, M.; Marzari, N.; Mauri, F.; Nguyen, N. L.; Nguyen, H. V.; Otero-de-la-Roza, A.; Paulatto, L.; Poncé, S.; Rocca, D.; Sabatini, R.; Santra, B.; Schlipf, M.; Seitsonen, A. P.; Smogunov, A.; Timrov, I.; Thonhauser, T.; Umari, P.; Vast, N.; Wu, X.; Baroni, S. Advanced Capabilities for Materials Modelling with Quantum ESPRESSO. J. Phys.: Condens. Matter 2017, 29, No. 465901.
- (70) Marzari, N.; Vanderbilt, D.; De Vita, A.; Payne, M. C. Thermal Contraction and Disordering of the Al(110) Surface. *Phys. Rev. Lett.* **1999**, 82, 3296–3299.

TRecommended by ACS

Hydrogen Production by Water Splitting with Support of Metal and Carbon-Based Photocatalysts

Anh Tuan Hoang, Xuan Phuong Nguyen, et al.

JANUARY 18, 2023

ACS SUSTAINABLE CHEMISTRY & ENGINEERING

READ 🗹

Machine Learning Assisted Analysis of Electrochemical H₂O₂ Production

Juyoung Leem, Xiaolin Zheng, et al.

MARCH 30, 2023

ACS APPLIED ENERGY MATERIALS

READ 🗹

Highly Efficient H_2O_2 Electrogeneration Enabled by Controlling the Wettability of Gas Diffusion Electrodes and the Reaction Pathway in Divided Cells

Jingwen Wang, Wenhui Wang, et al.

DECEMBER 27, 2022

ACS SUSTAINABLE CHEMISTRY & ENGINEERING

READ 🗹

Direct Quinone Fuel Cells

Yan Yurko and Lior Elbaz

JANUARY 20, 2023

JOURNAL OF THE AMERICAN CHEMICAL SOCIETY

READ 🗹

Get More Suggestions >